Acta Geochim (2026) 45:86–98
https://doi.org/10.1007/s11631-025-00769-8

ORIGINAL ARTICLE

Kumtag 061: A heavily shocked brachinite

Yuwei Zhang[1,2] · Dongliang Zhang[3] · Thomas Smith[4] · P. M. Ranjith[4] · Huaiyu He[4] · Guangming Song[5] · Yan Fan[6] · Shijie Li[1,7]

Received: 2 December 2024 / Revised: 23 January 2025 / Accepted: 20 February 2025 / Published online: 21 March 2025

Abstract Brachinite is a group of primitive achondrites that enables investigating the evolution of asteroids not fully differentiated in the early stage of the solar system. Kumtag 061 is a new meteorite sample collected on October 27, 2019, in Kumtag Desert, Xinjiang Province, China. The oxygen isotope composition ($\delta^{18}O = 5.086‰$, $\delta^{17}O = 2.396‰$, $\Delta'^{17}O = -0.298‰$) and petrologic and mineralogic analysis suggest Kumtag 061 is a heavy-impacted brachinite (S4–S5). The geochemical composition suggests Kumtag 061 represents a partial melting residue of the brachinite parent body. Based on the noble gas composition, the cosmic ray exposure age of Kumtag 061 is 60.9 ± 9.0 Ma. Combined with the gas retention ages, they indicate a (series of) thermal events on the parent body of brachinites before Kumtag 061 was ejected into space.

✉ Shijie Li
lishijielpsc@mail.gyig.ac.cn

1 Center for Lunar and Planetary Sciences, Institute of Geochemistry, Chinese Academy of Sciences, Guiyang 550081, China

2 University of Chinese Academy of Sciences, Beijing 100049, China

3 Key Laboratory of Metallogenic Prediction of Nonferrous Metals, Ministry of Education, School of Geosciences and Info-Physics, Central South University, Changsha 410083, China

4 State Key Laboratory of Lithospheric Evolution, Institute of Geology and Geophysics, Chinese Academy of Sciences, Beijing 100029, China

5 Beijing Institute of Spacecraft Environment Engineering, Beijing 100094, China

6 Xi'an Center, China Geological Survey, Xi'an 710054, China

7 Chinese Academy of Sciences Center for Excellence in Comparative Planetology, Hefei 230026, China

Keywords Brachinite · Impaction caused features · Partial melting residues of the parent body · Noble gases

1 Introduction

Primitive achondrites are meteorites with a near-chondritic bulk composition with non-chondritic structure (e.g., Collinet and Grove 2020) and still retain the geochemical features of their precursors (Mittlefehldt et al. 1998). Primitive achondrites record heating events and limited melting on their parent bodies, which may indicate partial melting without full differentiation into the multilayered structure, such as a metallic core, silicate mantle and crust. These meteorites provide an opportunity to investigate the evolution of the earliest stage asteroids (e.g., Day et al. 2015), one of the most important processes in the early solar system. Simultaneously, brachinite is an ultramafic group and is also the most oxidized group among primitive achondrites (Righter et al. 2016). Consequently, it provides an opportunity to investigate the evolutionary pathway of oxidized asteroid parent bodies.

Brachinites have a near-chondritic mineral abundance and mineral assemblage (e.g., Gardner-Vandy et al. 2013). Brachinites are mainly composed of olivine (~ 71%–96%, ~ $Fa_{27–36}$), with a significant amount of clinopyroxene (minor to ~ 15 vol%, ~ $En_{40–63}$, $Wo_{36–48}$) and plagioclase (0–10 vol%, $An_{15–33}$), and the minor minerals include trace amounts of orthopyroxene (none to ~20 vol%; $En_{40–63}$, $Wo_{36–48}$), Fe-sulfides (trace to ~7 vol%), chromite (none to ~5 vol%), phosphates (none to ~3 vol%) and metallic Fe–Ni (trace to ~2 vol%) (Keil 2014). Olivine in brachinites commonly displays triple junctions and exhibits medium- to coarse-grained textures, with sizes ranging from ~ 0.1 to 1.5 mm (e.g., Krot et al. 2014). Siderophile

element abundance patterns of brachinite range from ~ 0.01 to ~ 0.9 CI, while brachinites exhibit near-chondritic depletion in lithophile element abundance, such as Al, Ca, Rb, K, Ba, Na and LREE (e.g., Day et al. 2012). Generally, the bulk composition of brachinites is similar to that of chondrites, but their structure resembles that of achondrites.

The origin hypothesis of brachinites is still debated. The high CaO content of olivines in brachinites suggests that brachinites are igneous rocks derived from a differentiated asteroid (Mittlefehldt et al. 2003). However, several studies mentioned that brachinites represent partial melting residuals of the parent body due to their high siderophile elements abundance (e.g., Day et al. 2012). The crystallographic preferred orientation of olivines in several brachinite samples pointed to mineral accumulation, which also suggested that the brachinites were formed by partial melting, for example, EET 99402/99407 and ALH 84025 (Mittlefehldt et al. 2003), NWA 6112 and Divnoe #11 (Hasegawa et al. 2019).

The first brachinite (Brachina) was recovered in 1974, and up to 21 July 2024, only 62 meteorites had been classified as brachinite (Meteoritical Bulletin Database). The knowledge of brachinites and their parent body requires more samples to be constrained.

On October 27, 2019, a single meteorite weighing 2.54 kg was collected in the Kumtag Desert (coordinates: 41°16′9.20″ N, 93°14′14.10″ E). This meteorite was subsequently named Kumtag 061. In this paper, we classified it as brachinite according to its petrography, mineralogy and geochemistry features, and we also measured its noble gas composition and investigated the cosmic exposure and thermal histories. This data set provides a better understanding of the possible impact and thermal events that happened on the brachinite parent body.

2 Methods

2.1 Petrography, mineralogy and chemical composition

Petrographic analyses were carried out at the Institute of Geochemistry, Chinese Academy of Science (IGCAS), Guiyang, China. We first observed one thin section by using a Leica DM2700P optical microscope with both composite plane-polarized and cross-polarized light. Subsequently, we conducted petrographic and mineralogic investigations, and we analyzed two polished thick sections using the FEI Scio scanning electron microscope (SEM), with a voltage of between 15 and 20 kV, an electron beam current between 1.6 and 3.2 nA and a working distance between 7.0–15.5 mm.

The modal mineral abundance was measured using the Fiji application with different contrast ratios of different minerals, adjusting the threshold to distinguish a specific mineral and then calculating the area fraction. To avoid misidentification (e.g., the near contrast ratios of troilite and chromite), we calculate a selected area three times and then take the average of three different areas as the modal mineral abundance of the whole thin section.

Bulk major element composition was measured using a Thermal Fisher ARL Perform' X 4200 x-ray fluorescence spectrometry (XRF) in IGCAS. The instrument is equipped with OXSAS software and UniQuant program, and OXSAS analyzation was operated at the excitation power of 60 kV and 60 mA.

The mineral analyses for major element compositions were conducted at the Guilin University of Technology (GUT), Guilin, China. In situ mineral compositions (olivine, pyroxene, plagioclase and chromite) were measured using a JXA 8230 electron microprobe analyzer (EPMA), operated at an accelerating voltage of 15 kV, an electron beam current of 20 nA and 1–10 μm diameter.

Trace element contents were measured using a Thermal X series 2 inductively coupled plasma mass spectrometer (ICP-MS) equipped with a Cetac ASX-510 Autosampler from Guizhou Tongwei Analytical Technology Co., Ltd. Initially, the sample Kumtag 061 powder was digested (185 °C, for 72 h) in a Teflon crucible using 2 mL of 1:4 (v:v) HNO_3 and HF solution; residuum was redissolved with concentrated HNO_3. Then, the sample was dried and redissolved with 2N HNO_3. This step was repeated twice. Eventually, the solution was diluted to 1/4000 with 2% HNO_3. The final solution was then combined with internal spikes combined with 10 ppb o61Ni, 6 ppb Rh, In and Re (Tables 1, 2).

2.2 Noble gas

We prepared two parallel samples to analyze their bulk light noble gas concentrations and isotopic composition, weighing 8.07 mg and 6.24 mg, respectively. Noble gas measurements were carried out in the noble gas laboratory at the Institute of Geology and Geophysics, Chinese Academy of Science (IGGCAS), Beijing, China. The noble gas composition and isotopic ratios were measured using the multiple collector noble gas mass spectrometer Noblesse© from Nu Instruments. The analytical procedures followed the same steps as described previously in Ranjith et al. (2017). Samples were first cleaned with ethanol in an ultrasonic bath, dried, weighed and then loaded into the laser sample chamber of the noble gas extraction and purification line.

Calibrations were carried out using standard gases, which are of atmospheric composition except for He. The He standard is the "He Standard of Japan" (HESJ), with a $^3He/^4He$ ratio of 20.6 ± 0.1 Ra (Matsuda et al. 2002), where $Ra = 1.4 \times 10^{-6}$, representing the $^3He/^4He$ ratio of air. Sensitivities and instrumental mass discriminations were calculated based on the air measurements carried out at the time when the samples were analyzed. Blanks

Table 1 Bulk chemical composition of Kumtag 061

Element	Abundance	Method	Element	Abundance	Method
Li (μg g^{-1})	1.1	ICP-MS	Mo (μg g^{-1})	0.162	ICP-MS
Na (μg g^{-1})	1320	XRF	Sn (μg g^{-1})	0.063	ICP-MS
Mg (%)	15.7	XRF	Sb (μg g^{-1})	0.046	ICP-MS
Al (μg g^{-1})	3933	XRF	Cs (μg g^{-1})	0.008	ICP-MS
Si (%)	16.2	XRF	Ba (μg g^{-1})	7.1	ICP-MS
P (μg g^{-1})	510	XRF	La (μg g^{-1})	0.039	ICP-MS
S (μg g^{-1})	10,465	XRF	Ce (μg g^{-1})	0.082	ICP-MS
K (μg g^{-1})	182	XRF	Pr (μg g^{-1})	0.006	ICP-MS
Ca (μg g^{-1})	9798	XRF	Nd (μg g^{-1})	0.037	ICP-MS
Sc (μg g^{-1})	10.1	ICP-MS	Sm (μg g^{-1})	0.016	ICP-MS
Ti (μg g^{-1})	119	XRF	Eu (μg g^{-1})	0.017	ICP-MS
V (μg g^{-1})	83	ICP-MS	Gd (μg g^{-1})	0.026	ICP-MS
Cr (μg g^{-1})	4483	XRF	Tb (μg g^{-1})	0.006	ICP-MS
Mn (μg g^{-1})	2764	XRF	Dy (μg g^{-1})	0.039	ICP-MS
Fe (%)	22.7	XRF	Ho (μg g^{-1})	0.009	ICP-MS
Co (μg g^{-1})	334	ICP-MS	Er (μg g^{-1})	0.028	ICP-MS
Ni (μg g^{-1})	2078	XRF	Tm (μg g^{-1})	0.005	ICP-MS
Cu (μg g^{-1})	20.2	ICP-MS	Yb (μg g^{-1})	0.042	ICP-MS
Zn (μg g^{-1})	329	ICP-MS	Lu (μg g^{-1})	0.009	ICP-MS
Ga (μg g^{-1})	3.6	ICP-MS	Hf (μg g^{-1})	0.006	ICP-MS
Rb (ng g^{-1})	636	ICP-MS	Ta (μg g^{-1})	0.016	ICP-MS
Sr (μg g^{-1})	13.6	ICP-MS	Pb (μg g^{-1})	0.385	ICP-MS
Y (μg g^{-1})	0.243	ICP-MS	Th (μg g^{-1})	0.012	ICP-MS
Zr (μg g^{-1})	0.168	ICP-MS	U (μg g^{-1})	0.044	ICP-MS
Nb (μg g^{-1})	0.134	ICP-MS			

were frequently measured using the exact same extraction procedure as for the samples throughout the entire process. Therefore, the total amount of extracted gases was subsequently used for the blank. The following calculation was carried out based on the chemical composition of Kumtag 061.

The mass, noble gas concentrations and isotopic ratios of two duplicates (Kumtag 061-1 and Kumtag 061-2) of Kumtag 061 are presented in Table 3. The data were corrected for blanks, instrumental mass discrimination and interferences. The uncertainties regarding isotopic ratios are considerably smaller compared to those for isotopic concentrations because of optimization of the noble gas mass spectrometer. The uncertainties here are assumed to be in the range of 5%. We calculated the gas retention age based on the radiogenic composition concentration. The given uncertainty on T_4 is 1 SD. Considering the individual uncertainties of U and Th composition, which produced radiogenic ^{4}He, the uncertainties regarding the gas retention ages are taken as ~ 20% for T_4.

2.3 Oxygen isotope

The bulk oxygen isotopic compositions of Kumtag 061 were measured at the Oxy-Anion Stable Isotope Consortium, Louisiana State University (OASIC, LSU), using the same method as reported in Li et al. (2011, 2018, 2021). The standard we used to calculate oxygen isotope composition is V-SMOW (Vienna-Standard Mean Ocean Water). The measurements of silicate standards were NBS-28, UWG-2 and San Carlos olivine, with > 0.20‰ reproducibility for δ^{18}O and < 0.010‰ for Δ'^{17}O (Cowie and Johnston 2016). The $\delta^{17,18}$O and Δ'^{17}O are calculated by:

$$\delta^{17,18}\mathrm{O}(‰) = \left[\frac{\left(^{17,18}\mathrm{O}/^{16}\mathrm{O}\right)_{\mathrm{sample}}}{\left(^{17,18}\mathrm{O}/^{16}\mathrm{O}\right)_{\mathrm{V\,-\,SMOW}}} - 1\right] \times 1000$$

$$\Delta'^{17}\mathrm{O}(‰) = 1000\left[\ln\left(1 + \frac{\delta^{17}\mathrm{O}}{1000}\right) - 0.5305 \times \ln\left(1 + \frac{\delta^{18}\mathrm{O}}{1000}\right)\right.$$

3 Result

3.1 Petrography, mineralogy and geochemical composition

Kumtag 061 was covered by a gray-black fusion crust (Fig. 1). The section of Kumtag 061 shows a cataclastic texture, with olivine (79.0 vol%) as the main phase and relatively high abundance of pyroxene (8.5 vol%), troilite (7.7 vol%) and minor plagioclase (3.4 vol%), chromite. Fractures and darkening can be observed (Fig. 2a). Silicates (olivine, pyroxene and plagioclase) show obvious mosaic extinction and wavy extinction (Fig. 2b). Inclusions can be observed in most minerals. Only a few plagioclase grains contain

Table 2 Average compositions of minerals in Kumtag 061 analyzed by EPMA; the unit is wt% for oxides

	Olivine			Pyroxene (High-Ca)		Pyroxene (Low-Ca)			Chromite			Plagioclase	
	Avg (12)	SD		Avg (29)	SD	Avg (8)	SD		Avg (14)	SD		Avg (26)	SD
Na_2O	< 0.04			0.27	0.08	0.04	0.02		0.05	0.05		7.27	0.28
SiO_2	37.53	0.19		54.61	0.57	55.61	0.30		0.06	0.07		60.87	1.46
Al_2O3	< 0.04			0.51	0.29	0.21	0.03		10.09	0.35		23.56	1.04
MgO	32.07	0.28		16.44	1.83	25.04	0.53		3.59	0.30		0.51	0.39
CaO	0.04	0.03		20.19	3.94	1.39	0.49		0.04	0.12		6.61	0.37
Cr_2O_3	< 0.04			< 0.04		< 0.04			55.83	1.14		0.05	0.20
P_2O_5	0.05	0.02		< 0.04		< 0.04			< 0.04			< 0.04	
MnO	0.35	0.12		0.19	0.07	0.36	0.06		0.40	0.06		< 0.04	
K_2O	< 0.04			< 0.04		< 0.04			< 0.04			0.10	0.01
FeO	31.48	0.28		8.45	2.21	18.82	0.34		29.24	0.82		1.40	1.25
TiO_2	< 0.04			0.11	0.04	< 0.04			1.00	0.10		< 0.04	0.02
NiO	< 0.04			< 0.04		< 0.04			0.02	0.02			
Total	101.58	0.34		100.81	0.77	101.54	0.46		100.32	0.85		100.44	1.15
Fa	35.5	0.4	Fs	13.3	3.4	28.8	0.6	Cr/(Cr + Al)	0.8	0.0	An	33.2	1.7
Fo	64.5	0.4	Wo	40.7	8.0	2.7	1.0	Fe/(Fe + Mg)	0.8	0.0	Ab	66.1	1.7
Fe/Mn	74.9	25.8	En	46.0	4.8	68.4	1.1				Or	0.6	0.1

Only one Cr_2O_3 content value of olivine in Kumtag 061 was detected

The '< 0.04' stands for lower than the limit of detection

Table 3 Analyzed mass of the studied samples and their He, Ne and Ar concentrations and isotopic ratios

Samples	Mass (mg)	^3He ($10^{-8}cm^3$ STP/g)	$^3He/^4He$	^{20}Ne ($10^{-8}cm^3$ STP/g)	$^{20}Ne/^{22}Ne$	$^{21}Ne/^{22}Ne$	^{38}Ar ($10^{-8}cm^3$ STP/g)	$^{36}Ar/^{38}Ar$	$^{40}Ar/^{36}Ar$
Kumtag 061–1	8.07	92.61 ± 4.63	0.097 ± 0.001	17.06 ± 0.85	0.850 ± 0.004	0.950 ± 0.050	2.10 ± 0.11	2.867 ± 0.005	174 ± 9
Kumtag 061–2	6.24	99.64 ± 4.99	0.183 ± 0.005	17.19 ± 0.86	0.839 ± 0.004	0.935 ± 0.034	3.64 ± 0.18	2.919 ± 0.005	209 ± 10

inclusions. The inclusion minerals contain olivine, pyroxene, plagioclase and troilite; these are mainly tiny troilite grains (details are described in the following text). Some enclosed minerals preserve their igneous texture, while others show an embayed texture or appear as tiny blebs (Fig. 3a).

Most olivines present as fine-grained assemblages (~ 10–15 μm), with fractures cut through olivine grains (Fig. 2b). According to the mineral composition listed in Table 2 (hereafter the same), the Fa content of olivine ($Fa_{34.8–36.2}$) is similar to that of the brachinite group meteorites ($Fa_{26–37}$, Keil 2014). Fe/Mn ratios (65.3–84.5) are within the average range of the brachinite (59.0–81.3, Keil 2014), with three relatively higher Fe/Mn ratios (91.4, 96.4 and 98.7 respectively). The CaO content of olivines varies from 0.02 to 0.11 wt%, with an average of 0.04 wt%.

Pyroxenes in this sample primarily present as high-Ca pyroxene ($Fs_{10.5–23.7}$, $En_{43.3–61.5}$ and $Wo_{14.8–45.5}$) and a small number of low-Ca pyroxene grains ($Fs_{28.3–29.4}$, $En_{66.0–69.9}$ and $Wo_{2.1–5.1}$). Low-Ca pyroxene mainly presents as anhedral grains, and high-Ca pyroxene presents as both subhedral and anhedral grains. The sizes of pyroxene grains vary from ~ 50 to ~ 200 μm, and the sizes do not correlate with grain shapes. Subhedral pyroxene grains maintain igneous straight crystal boundaries (Fig. 3a); simultaneously, anhedral grains show an embayed texture (Fig. 3a) and a lenticular-shaped texture (Fig. 3a), also presenting as elongated grains (Fig. 3a, b). All three shapes of pyroxenes have inclusions inside, and the compositions of these inclusions are olivine, plagioclase and troilite.

Plagioclases present as subhedral to embayed textured grains and elongated grains (Fig. 3a, c), with $An_{29.2–35.6}$, $Ab_{63.8–70.1}$ and $Or_{0.5–0.8}$. The grain size range of plagioclases is also relatively large, varying from ~ 0.5 to ~ 200 μm. Only a few enclosed grains are found in plagioclase.

Chromium content (Cr_2O_3) in chromite varies between 54.17–57.56 wt%, the average Cr/(Cr + Al) ratio is 0.8, and

Fig. 1 The location in Kumtag Desert, Xinjiang Province, China, where Kumtag 061 was collected. The surface of this meteorite was covered by a black fusion crust

the average Fe/(Fe + Mg) ratio is 0.8. Chromite usually presents as ~ 30 to ~ 100-μm subhedral grains. Most chromite grains grow with troilite (Fig. 3a, d).

Troilites mostly exist as tiny spherical or hemispherical grains (~ 0.1–0.5 μm), pervade throughout the whole thin section and fill the fractures between minerals exhibiting a grid-like structure (Fig. 3a). Some relatively large irregular grains (~ 10 to ~ 100 μm) are also present, and some have been affected by terrestrial weathering (Fig. 3e). Several large troilite grains present with chromite (Fig. 3d). Thin troilite veins cut through several pyroxene and plagioclase grains; simultaneously, some veins are blocked by mineral grains (Fig. 3a).

The bulk chemical composition is shown in Table 1. The bulk composition of Kumtag 061 is 34.60 wt% SiO_2, 32.51 wt% Fe_2O_3 and 26.11 wt% MgO, with low Al_2O_3 (0.74 wt%). The element results are normalized with CI chondrite and magnetism; the normalized pattern is shown in Fig. 4. Compared to other brachinite samples, Kumtag 061 has a relatively low rare earth element (REE) abundance. The La/Yb ratio is 0.93, and the Nb/Ta ratio is 8.65. The REE pattern of Kumtag 061 whole rock shows enrichment of Eu and slight enrichment of heavy rare earth elements (HREEs). The abundance of Ba (7.09 ppm) and Pb (0.385 ppm) of Kumtag 061 is also relatively low.

3.2 Oxygen isotopes

The average bulk oxygen isotope composition of three parallel Kumtag 061 samples is as follows: $\delta^{18}O$ composition is 5.086‰ ± 0.20‰, $\delta^{17}O$ composition is 2.396‰ ± 0.15‰, and $\Delta'^{17}O$ composition is − 0.298‰ ± 0.010‰. Errors here are SE represented by long-term standard reproducibility.

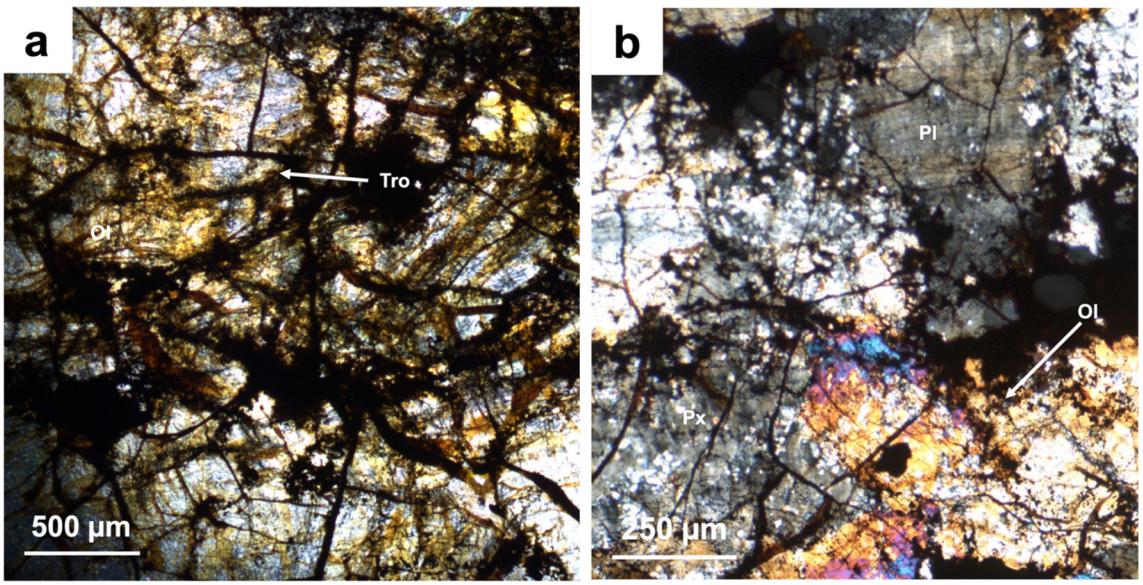

Fig. 2 Optical microscope photo of Kumtag 061. **a** Composite plane-polarized light image of Kumtag 061 shows obvious shock darkening features. Olivines present a slight interference color; therefore, this thin section was not polished on both sides. **b** Composite cross-polarized light image of the thin section of Kumtag 061. Olivine and plagioclase show mosaic extinction and wavy extinction

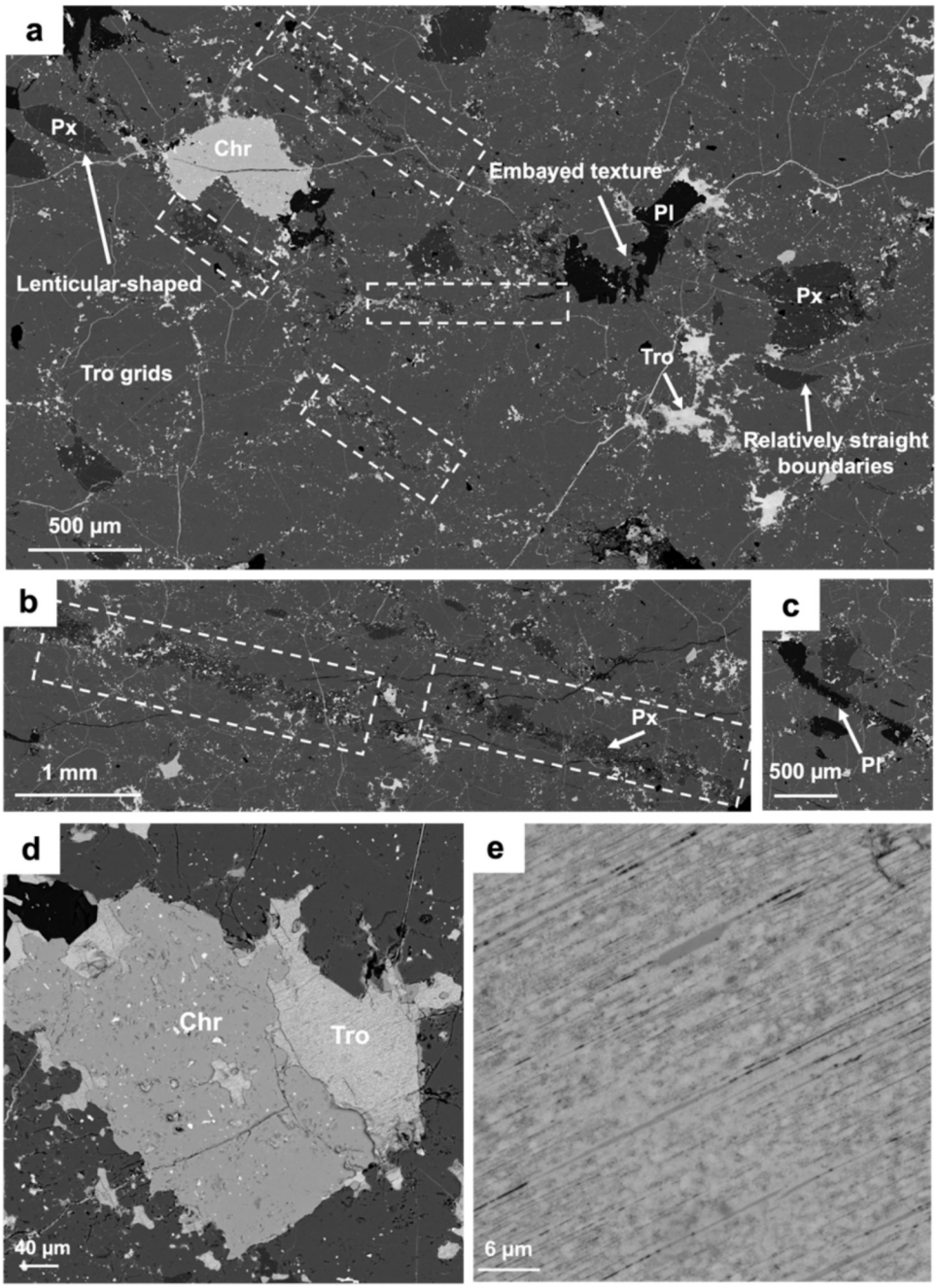

Fig. 3 Backscatter electron (BSE) images of Kumtag 061. **a** Olivines present as a large gray area. Troilites form grids in cracks, and thin veins cut through the mineral grains, also presenting as tiny spherical or ellipsoidal grains. Olivine, plagioclase and troilite grains were enclosed in a pyroxene grain, and these inclusion minerals also enclosed other minerals. Lenticular-shaped pyroxene grains can be observed. The boundaries of minerals, for example, pyroxene, show embayed texture; simultaneously, several grains show relatively straight boundaries and maintain an igneous texture. The elongated pyroxene and plagioclase grains are marked by dashed boxes. **b** Elongation of pyroxene grains, tiny troilites scattered within. **c** Plagioclase shows elongated features, with a small amount of enclosed troilites. **d** Chromite grain and weathered troilite. **e** Weathered troilite grain. Px. pyroxene, Pl. plagioclase, Tro. troilite, Chr. chromite

3.3 Noble gases and chronology

We measured the concentration and isotopic ratios of the light noble gases (He, Ne and Ar) in Kumtag 061 and subsequently calculated its cosmic ray exposure (CRE) age and gas retention age.

For the component deconvolution, we make the following assumptions: (1) ^{3}He is assumed to be entirely cosmogenic; (2) the total ^{4}He composition is the sum of radiogenic ^{4}He ($^{4}He_{rad}$) and cosmogenic ^{4}He ($^{4}He_{cos}$), with the assumption $(^{4}He/^{3}He)_{cos}$ is ~ 5 (Eugster and Michel 1995); (3) for neon, we adopt a cosmogenic $(^{20}Ne/^{22}Ne)_{cos} \sim 0.80$, $(^{20}Ne/^{22}Ne)_{tr} \sim 9.80$ and $(^{21}Ne/^{22}Ne)_{tr} \sim 0.029$; (4) for argon, we adopt $(^{36}Ar/^{38}Ar)_{tr} = 5.32$ and $(^{36}Ar/^{38}Ar)_{cos} = 0.65$; (5) different trapped noble gas components are assumed to be air. The results are shown in Table 4.

We calculate the cosmic ray exposure (CRE) ages T_3, T_{21} and T_{38} based on the concentration of cosmogenic $^{3}He_{cos}$, $^{21}Ne_{cos}$ and $^{38}Ar_{cos}$, respectively. To account for uncertainties in the calculation of production rates and the chemical composition of the sample, a 15% error was applied to all CRE ages. For clarity, we add parentheses to the CRE

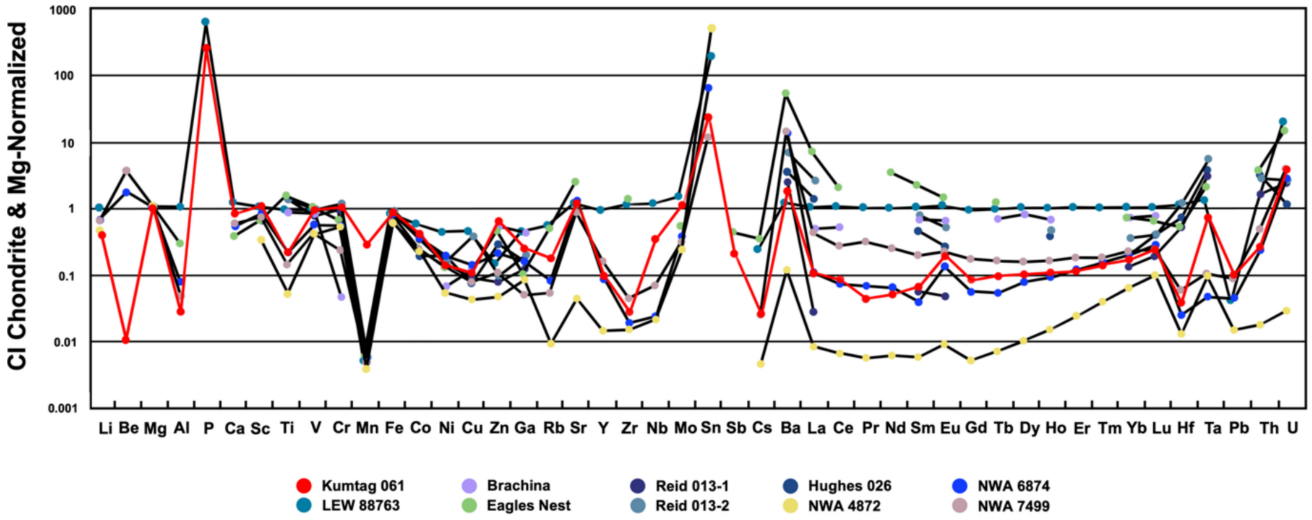

Fig. 4 Bulk chemical composition of Kumtag 061, normalized to magnesium and CI chondrites [composition given by McDonough and Sun (1995)]. Data sources are: Hughes 026 and Reid 013 (Goodrich et al. 2010); Brachina (Johnson, 1977; Nehru et al. 1983); Eagle's Nest (Swindle et al. 1998), NWA 6874 and NWA 7499 (Nicklas et al. 2023), LEW 88763 (Day et al. 2015); NWA 4872 (Hyde et al. 2014). The Mg abundance of NWA 4872 is the average MgO in the primary mineral phase (olivine, pyroxene, Cr-spinel, chlorapatite and merrillite), calculated from the data in Hyde et al. (2014)

Table 4 Cosmogenic He, Ne and Ar concentrations (in 10^{-8} cm^3 STP/g) and isotopic compositions. Measured ^{40}Ar is assumed to be the sum of radiogenic and trapped components

Samples	$^3He_{cos} = {}^3He_m$ (10^{-8}cm^3 STP/g)	^4He_m (10^{-8}cm^3 STP/g)	$^4He_{rad}$ (10^{-8}cm^3 STP/g)	$^{21}Ne_{cos}$ (10^{-8}cm^3 STP/g)	$(^{22}Ne/^{21}Ne)_{cos}$	$^{36}Ar_{cos}$ (10^{-8}cm^3 STP/g)	$^{38}Ar_{cos}$ (10^{-8}cm^3 STP/g)	^{40}Ar (10^{-8}cm^3 STP/g)
Kumtag 061–1	92.61 ± 4.63	952 ± 48	489 ± 24	19.07 ± 0.95	1.049 ± 0.001	0.737 ± 0.037	1.133 ± 0.057	1048 ± 52
Kumtag 061–2	99.64 ± 4.99	571 ± 29	72.5 ± 3.6	19.15 ± 0.96	1.066 ± 0.001	1.251 ± 0.063	1.924 ± 0.096	2221 ± 111

ages, which are considered doubtful, primarily because of the heterogeneity in the distribution of the target elements to produce ^{38}Ar (such as Fe, Ni and Ca). The average T_3, T_{21} and T_{38} age of Kumtag 061 is 39.4 ± 5.9 Ma, 60.0 ± 9.0 Ma and 42.8 ± 6.4 Ma, respectively. The adopted CRE age (highlighted in bold) is the average of calculated T_{21} CRE ages (the details are explained in the discussion).

The gas retention T_4 is calculated based on the concentrations of radiogenic ^{4}He, which are 793 ± 158 Ma and 125 ± 25 Ma, respectively (Fig. 5).

4 Disscussion

4.1 Kumtag 061 is influenced by a heavy impact event and melting

The bulk oxygen isotope composition of Kumtag 061 (δ^{18}O of 5.086‰, δ^{17}O of 2.396‰, Δ'^{17}O of − 0.298‰) is in the range of brachinites (δ^{18}O from 2.37‰ to 5.86‰, δ^{17}O from − 0.03‰ to 2.86‰, Δ'^{17}O from − 0.39‰ to − 0.09‰, according to Keil 2014) and also shows a consistent δ^{17}O/δ^{18}O trend with other brachinite samples (Fig. 6). These features suggest that Kumtag 061 originates from the same parent body as other brachinites. Mineral abundance and mineral composition are also consistent with Kumtag 061 being a brachinite. EPMA analysis compositions of olivine, plagioclase, pyroxene and chromite are similar to those of brachinites. The Fa value of olivine (34.8–36.2 mol%), Fs value (10.5–23.7 mol% for high-Ca pyroxene and 28.3–29.4 mol% for low-Ca pyroxene), En value (43.3–61.5 mol% for high-Ca pyroxene and 66.0–69.9 mol% for low-Ca pyroxene) and Wo value (14.8–45.5 mol% for high-Ca pyroxene and 2.1–5.1 mol% for low-Ca pyroxene) of pyroxene and An value of plagioclase (29.2–35.6 mol%) are in the range of typical brachinite values (olivine $Fa_{27–37}$; orthopyroxene $En_{69–74}$, $Wo_{2–4}$, clinopyxroxene $En_{40–63}$, $Wo_{36–48}$; plagioclase $An_{9–44}$, according to the summary in Keil 2014). The bulk molar FeO/MnO ratio is 80.8, and the bulk molar FeO/MgO ratio

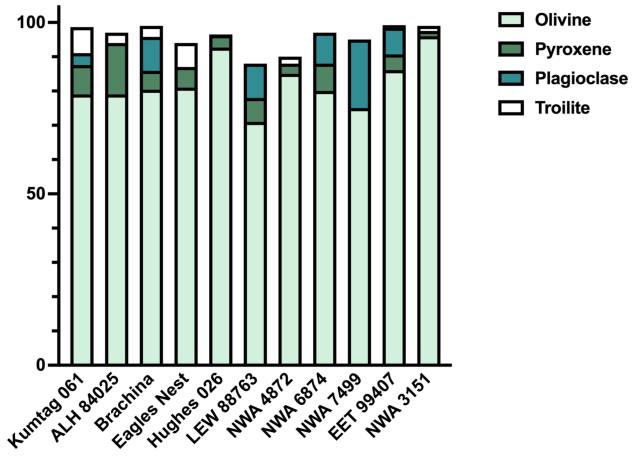

Fig. 5 Modal mineral composition of brachinites (vol%). The modal abundance of pyroxene was calculated as the sum of clinopyroxene and orthopyroxene. Pyroxene, plagioclase and sulfides of several samples do not appear in this figure, because their compositions are described as minor, rare, trace, present and none. Sulfide in Eagle's Nest is the sum of Fe sulfides, oxides and ~ 5% altered materials. Data source: ALH 04925 (Warren and Kallemeyn 1989), Brachina (Nehru et al. 1979), Eagle's Nest (Kring and Boynton 1992; Swindle et al. 1998), Hughes 026 (Nehru et al. 1996), LEW 88763 (Swindle et al. 1998), NWA 3151 (Gardner-Vandy et al. 2013), NWA 4872 (Rumble et al. 2008), NWA 6874 (Ruzicka et al. 2014) and NWA 7499 (Ruzicka et al. 2015)

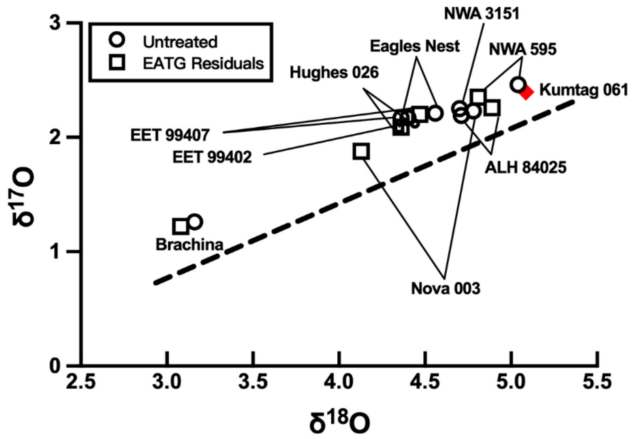

Fig. 6 The bulk oxygen isotopic composition ($\delta^{18}O$ versus. $\delta^{17}O$) of Kumtag 061. Data source is Greenwood et al. (2012). EATG residuals are brachinite samples leached with an ethanolamine thioglycolate solution to eliminate the terrestrial weathering products. The dashed line represents the oxygen isotopic fractionation trend of brachinites

is 0.6, showing chondritic features (Goodrich and Delaney 2000).

Kumtag 061 shows heavier shock-induced features. Olivine presents mosaic extinction, wavy extinction and obvious shock darkening (Fig. 2a). Troilite is present in grids in the fractures between olivines (Fig. 3a), which were caused by impaction. Several troilites are irregular with larger granularity; most troilites in Kumtag 061 are present as tiny spherical or ellipsoidal grains (Fig. 3a), formed by impaction-induced decomposition and gasification and then condensed in the release progress (e.g., Rubin 2002; Li et al. 2021). The relatively low content of enclosed troilites in plagioclase may be due to the melting point of plagioclase. These phenomena can also give information about the process by which Kumtag 06l was affected by a heavy impact, which is not common in brachinite samples. We semi-quantitatively justify that the shock stage of Kumtag 061 reached S4–S5 according to the mosaicism of olivines and shock darkening (Stöffler et al. 1991). Though the plagioclase in EET 99402 and EET 99407 (a pair of brachinites) was shocked to maskelynite (Mittlefehldt et al. 2003), the shock-caused feature in these samples was not remarkable in Kumtag 061.

Despite the impact-melt features, Kumtag 061 also indicates possible early-stage melting. The formation mechanism of brachinites remains debated. Two mechanisms are generally evoked: partial melt residues (e.g., Day et al. 2012) and olivine accumulation (e.g., Hasegawa et al. 2019; Meunier-Mili et al. 2024). As primitive achondrites, the residues result from low-degree melting of the brachinite parent body. Igneous fractionation features usually present as a near-constant Fe/Mn ratio and a wide range of Fe/Mg ratios (Goodrich et al. 2017), the molar Fe/Mn ratio of Kumtag 061 is 65.4–96.9, and molar Fe/Mg is 0.2, suggesting low degrees of melting within this sample (e.g., Goodrich et al. 2017). The embayed texture of minerals (Fig. 3a) pointed to melting and recrystallization. Elongation of pyroxene and plagioclase (Fig. 3a–c) also points to melting, representing possible migration of the melt. The CaO contents in olivine (0.02–0.11 wt%, with an average of 0.04 wt%) are relatively lower than in other brachinites (with an average of 0.15 reported by Mittlefehldt et al. 2003), indicating that it may be the result of limited melt migration (Goodrich et al. 2017). The relatively low CaO content in the olivines of Kumtag 061 may be due to the activity of large-ion lithophile elements (LILEs), and calcium tends to enter the melts. Low CaO content represents metamorphic/melt-residue olivines (Mittlefehldt et al. 2003). Brachinites show different degrees of aluminum depletion (Keil 2014). The Al abundance in Kumtag 061 (Fig. 4) may also be affected by melting migration, causing a relatively intense depletion of aluminum. The deplted REE composition also supports Kumtag 061 as a partial melting residue. Kumtag 061 also shows the same trend as NWA 4872 and NWA 6874 (Fig. 4), which are classified as a residuum after partial melting (Hyde et al. 2014; Nicklas et al. 2023). These phenomena suggest that Kumtag 061 has experienced a melting progress and melt migration, which may be caused by earlier impact events, simultaneously, still representing the residue of partial melting caused by geochemical features.

4.2 Cosmic ray exposure age of Kumtag 061

Cosmic rays produce cosmogenic noble gas nuclides (e.g., ^{3}He, ^{21}Ne and ^{38}Ar) on the surface of celestial bodies, which accumulate over time. Consequently, the concentration of cosmogenic noble gases can be used to calculate the time when small meteorites were ejected from their parent bodies, the so-called cosmic ray exposure (CRE) age.

The two duplicates have Ne ratios that are almost purely cosmogenic, i.e., with only a small contribution from a trapped component (here assumed to be air) (Fig. 7). We ruled out the presence of solar wind (SW), Q and P3 and only considered a binary mixture of cosmogenic and trapped (air) components. Due to the lack of specific equations for calculating the production rates of brachinites, we calculated these CRE ages according to the chemical composition of Kumtag 061 and the calculation method of production rate systematics in Eugster (1988) and Eugster and Michel (1995). The CRE ages (T_3, T_{21} and T_{38}) of Kumtag 061 are reported in Table 5. The T_3/T_{21} ratio is in the range of 0.63–0.68. This ratio indicates an apparent depletion of ^{3}He after the ejection of Kumtag 061 from its parent body. In addition, troilites are also affected by terrestrial weathering, which may therefore influence the amount of ^{3}He. The cosmogenic argon concentrations are significantly different in both duplicates (see Table 4), resulting in variations of the calculated T_{38}. Though noble gases experience possible diffusion loss both on the surface of the earth and in the space environment (e.g., Tremblay et al. 2014; Shuster and Cassata 2015), we observe a good agreement between ^{3}He and ^{21}Ne concentrations in both duplicates, suggesting that the difference observed in ^{38}Ar concentration may be caused by a variation in the chemistry within the sample.

Table 5 Nominal cosmic ray exposure (CRE) ages (T_3, T_{21} and T_{38}) of Kumtag 061 based on cosmogenic $^{3}He_{cos}$, $^{21}Ne_{cos}$, and $^{38}Ar_{cos}$ concentrations, respectively

Samples	T_3 (Ma)	T_{21} (Ma)	T_{38} (Ma)	$T_{adopted}$ (Ma)
Kumtag 061–1	37.9 ± 5.7	59.9 ± 9.0	(25.2 ± 3.8)	
Kumtag 061–2	40.8 ± 6.1	60.1 ± 9.0	42.8 ± 6.4	
Adopted CRE age	**39.4 ± 5.9**	**60.0 ± 9.0**	**42.8 ± 6.4**	**60.0 ± 9.0**

Cosmic ray exposure age was calculated based on the chemical composition of Kumtag 061, and the equation used to calculate the production rate was according to P_3 (Cressy and Bogard 1976), the equation for P_{21} was described in Eugster (1988) and P_{38} (Eugster and Michel 1995)

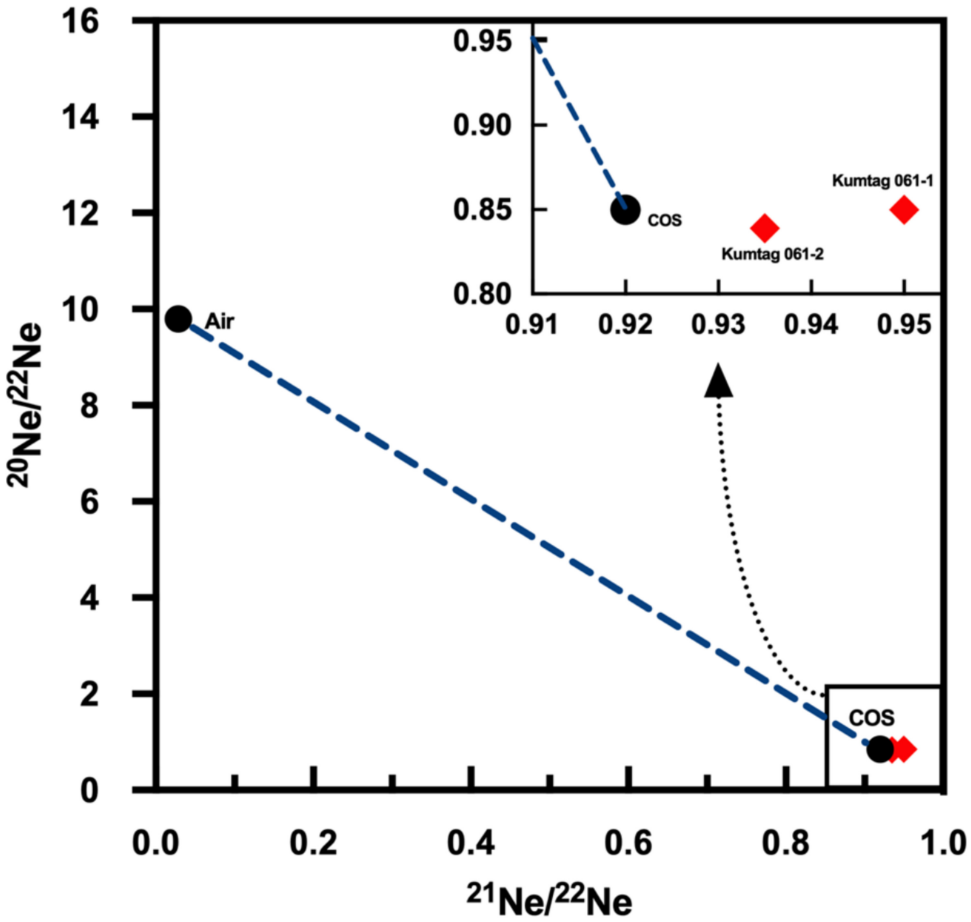

Fig. 7 Neon three-isotope plot of Kumtag 061. The isotopic compositions of galactic cosmic rays (COS, Busemann et al. 2000) and trapped components [after excluding other trapped components, such as solar wind (SW; Heber et al. 2012), Q (Busemann et al. 2000) and P3 (Huss and Lewis 1994)]; here, we take atmospheric Ne ($^{21}Ne/^{22}Ne)_{Air}$ ~ 0.029 and ($^{20}Ne/^{22}Ne)_{Air}$ ~ 9.80, Eberhardt et al. 1965)

The variation in T_{38} is mainly influenced by the contents of potassium and calcium (e.g., Freundel et al. 1986; Eugster and Michel 1995), which are mainly contained in plagioclase and pyroxene. As shown in Fig. 5, the modal composition of plagioclase in Kumtag 061 is relatively low (though Kumtag 061 shows a bulk-positive Eu anomaly, which may be caused by tiny and unobserved plagioclase grains, as described in Nehru et al. 1983); this may be caused by a difference in the target element compositions of samples. The measured ^{40}Ar concentration of the two duplicates confirms this assumption. As shown in Fig. 7, the neon isotopic composition of Kumtag 061 was barely affected by trapped neon. Therefore, we adopt a CRE age of 60 ± 9.0 Ma for Kumtag 061, based on T_{21}.

Previous studies show that six peaks were identified in the brachinite CRE age histogram, hence indicating six major impact events on the brachinite parent body (at approximately 4, 9, 25, 38, 50 and 65 Ma; details are shown in Fig. 8). The calculated exposure age of Kumtag 061 is approximately 60 Ma, with 15% uncertainty, which falls within the range of CRE ages reported for Eagle's Nest (Swindle et al. 1998), EET 99402 (Patzer et al. 2003), NWA 4969, 4876 and NWA 4882 (Beard 2018). These meteorites may be ejected from a series of impact events during the time interval of 20 Ma.

4.3 Thermal history of Kumtag 061

Generally, the crystallization age of brachiniteS is considered to be approximately 4.5 Ga, though several samples showed alteration due to impact, which may have caused a relatively young crystallization age in the brachinite group. The ^{53}Mn-^{53}Cr age of Brachina is 4563.7 ± 0.9 Ma (Wadhwa et al. 1998), whereas EET 99402 shows a ^{39}Ar-^{40}Ar age of 4130 ± 60 Ma because of impact heating and degassing (Mittlefehldt et al. 2003). According to the crystallization age of brachinites and the petrologic features of Kumtag 061 (e.g., embayed texture), we suggest that this sample possibly experienced melting and recrystallizing. These processes, especially melting, would cause a loss of radiogenic noble gas, which was enclosed in minerals. In this case, T_4 and T_{40} could be used to reveal the thermal history of the sample. The gas retention age can constrain the upper limit of the

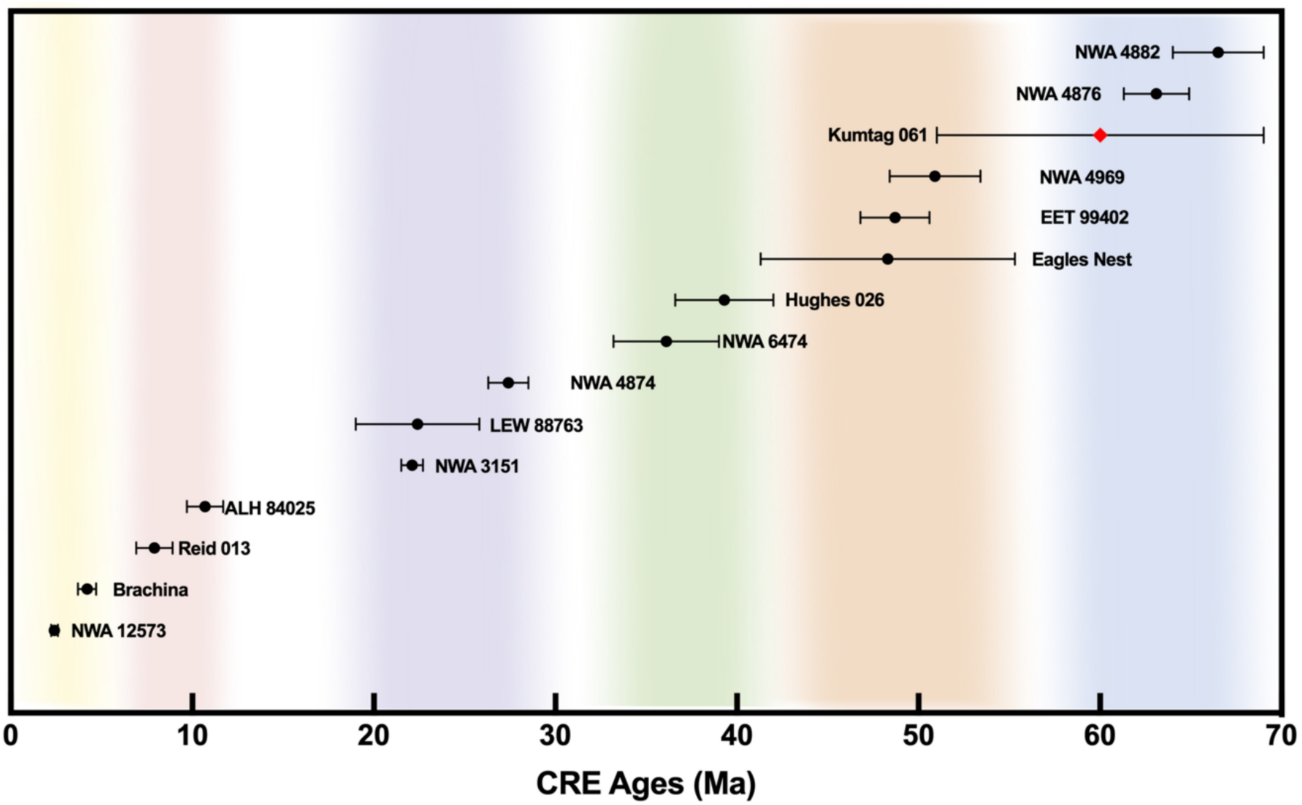

Fig. 8 Cosmic ray exposure (CRE) age of brachinites. Here, we use T21 to represent the CRE age of the samples. The CRE ages of Brachina, Reid 013, ALH 84025, LEW 88763, Hughes 026 and Eagle's Nest are from Beard (2018), which recalculated the CRE ages using literature values. The other data are from NWA 12573 (Smith et al. 2023), Brachia (Ott et al. 1985), Reid 013, Hughes 026 and EET 99402 (Patzer et al. 2003), ALH 84025 (Ott et al. 1993), NWA 3151, NWA 4874, NWA 6474, NWA 4969, NWA 4876 and NWA 4882 (Beard 2018), LEW 88763 and Eagle's Nest (Swindle et al. 1998)

thermal event when assuming that the radiogenic gas was totally lost during melting.

We assumed the total ^{40}Ar concentration is the sum of trapped and radiogenic ^{40}Ar to calculate the gas retention age T_{40}. After deducting the trapped ^{40}Ar, the radiogenic ^{40}Ar is negative. Hence, it is not available for T_{40} calculation.

Except for radioactive uranium and thorium, radioactive samarium may also affect the concentration of radiogenic ^{4}He. As we discussed before, Kumtag 061 is a possible partial melting residuum, and the concentration of incompatible elements is relatively low (e.g., Sm = 156 ng g^{-1}). Considering the abundance of radioactive ^{147}Sm and the low abundance of plagioclase in Kumtag 061 (as shown in Fig. 5), we proposed that radioactive Sm inconspicuously affects the radiogenic ^{4}He concentration. For radiogenic $^4He_{rad}$, the gas retention age T_4 is 793 ± 158 Ma and 125 ± 25 Ma, respectively.

Noble gases are lost to different degrees because of the different melting points of occurrence minerals in melting events. As mentioned before, we assume that the measured noble gases were reset after the melting events, i.e., radiogenic noble gases produced prior to impact were totally lost because of melting. Ideally, different radiogenic noble gases should represent the same gas retention age, which indicates that these noble gases were not lost or fully lost. However, the different T_4 in these two duplicates could be caused by sample variation and also could be influenced by the loss of helium during the exposure in space according to the T_3/T_{21} ratios (0.63–0.68). Therefore, the gas retention ages of Kumtag 061 cannot represent a specific time node of thermal events, only suggesting the thermal event happened on the brachinite parent body before Kumtag 061 was ejected.

4.4 The preatmospheric size of Kumtag 061

Due to the high speed (~ 10–70 km/s) at which meteorites enter the atmosphere of earth, friction generates heat which in return causes severe ablation of meteorites, resulting in 80%–90% mass loss (Bhandari et al. 1980). By assuming that this process is analogous to a symmetric ablation, we can use the cosmogenic $(^{22}Ne/^{21}Ne)_{cos}$ as a proxy for determining the preatmospheric size and for estimating the shielding depth of Kumtag 061.

Here, we take the average $(^{22}Ne/^{21}Ne)_{cos}$ ratio of 1.0575 ± 0.001 in Kumtag 061-1 (1.049 ± 0.001) and Kumtag 061-2 (1.066 ± 0.001). Based on the model prediction of Leya and Masarik (2009), the radius range of Kumtag 061 can be calculated. The preatmospheric mass of Kumtag 061 is derived by using the equations from Bhandari et al. (1980), which leads to an estimated mass of 171 ± 26 kg. According to the average bulk density of brachinite (3.48 g/cm^3, Keil 2014), the preatmospheric radii of Kumtag 061 are calculated to be 23 ± 1 cm.

The total mass of Kumtag 061 is 2.54 kg. According to our calculation, this sample experienced a relatively serious mass loss, only preserving approximately 1.5% recovered, which may have led to the lack of paired samples or other brachinite samples found in this area, which was subsequently reported by the meteorite hunters.

4.5 The inspiration for finding a brachinite in Kumtag Desert

Desert areas are ideal meteorite-collecting regions due to their special climate and geographic characteristics. About 30% of meteorites were collected from hot deserts (Drouard et al. 2019). Hot desert meteorites also provide information about the distribution of meteorite showers and the fragmentation process of bolide during atmospheric entry (e.g., Pourkhorsandi et al. 2019).

Kumtag Desert is located in the east of Xinjiang Province, China. Aside from widely discovered ordinary chondrites, several rare categories of meteorites were also found in Kumtag Desert, including one CO_3 chondrite (Shanshan 002), one EL7 chondrite (Baqiangzi), one ureilite (Loulan Yizhi 001), one eucrite (Yiwu 001), one diogenite (Lop Nur 001) and the brachinite, Kumtag 061 (Fan et al. 2022). Compared to other mature dense meteorite collection areas (DCAs) in Northwest Africa, this area still lacks study. According to the discoveries of these meteorites, in particular Kumtag 061, a brachinite sample, we suggest that the Kumtag DCA, which is defined by the Meteoritical Society, is of great interest for further meteorite collection work and meteoritical research.

5 Summary and conclusions

The new brachinite Kumtag 061, which was collected in the Kumtag Desert region in Xinjiang, China, was mainly shaped by melting and impaction. Kumtag 061 shows mosaic extinction, pervasive tiny troilite grains and thin troilite melt veins, which indicate one or a series of heavy impact events happened on the parent body of brachinites. These features of Kumtag 061 suggest that the brachinite parent body suffered a higher degree of impact than previously reported. The embayed texture of silicate point melting, the relatively low bulk Al content, CaO content in olivine and REE abundance of Kumtag 061 indicate this sample represents a partial melting residue of the brachinite parent body.

The CRE age of Kumtag 061 is 60.0 ± 9.0 Ma, in agreement with two of the peaks in the CRE age histogram of brachinites. The T_3/T_{21} ratio indicates that Kumtag 061 experienced cosmogenic ^{3}He ($^3He_{cos}$) loss after the sample was ejected from its parent body. The preatmospheric radii of Kumtag 061 are calculated to be 23 ± 1 cm.

Acknowledgements This work is supported by the Project of High-level Innovative Talents of Guizhou Province (GCC[2022]017-1) and the National Natural Science Foundation of China (grant no. 42173046). We thank Prof. Yongbo Peng for carrying out the bulk oxygen isotopic composition measurement. We thank the meteorite hunters Pengli Chen and Zijian Wang for providing information about the sample and the strewn field.

Author contributions Yuwei Zhang: writing—original draft, visualization, methodology, investigation, formal analysis, data curation, conceptualization; Dongliang Zhang: writing—review and editing; Thomas Smith: writing—review and editing, methodology; P.M. Ranjith: writing—review and editing, methodology; Huaiyu He: writing—review and editing, methodology; Guangming Song: writing—review and editing; Yan Fan: writing—review and editing; Shijie Li: writing—review and editing, methodology, formal analysis, methodology, investigation, funding acquisition, conceptualization.

Declarations

Conflict of interest The authors declare that they have no conflict of interest.

References

Beard S (2018) Noble gas chronology of meteorites: brachinites, ureilites, and chelyabinsk.

Bhandari N, Lal D, Rajan RS, Arnold JR, Marti K, Moore CB (1980) Atmospheric ablation in meteorites: a study based on cosmic ray tracks and neon isotopes. Nucl Tracks 4(4):213–262. https://doi.org/10.1016/0191-278X(80)90037-2

Busemann H, Baur H, Wieler R (2000) Primordial noble gases in "Phase Q" in carbonaceous and ordinary chondrites studied by closed-system stepped etching. Meteorit Planet Sci 35(5):949–973. https://doi.org/10.1111/j.1945-5100.2000.tb01485.x

Collinet M, Grove TL (2020) Formation of primitive achondrites by partial melting of alkali-undepleted planetesimals in the inner solar system. Geochim Cosmochim Acta 277:358–376. https://doi.org/10.1016/j.gca.2020.03.004

Cowie BR, Johnston DT (2016) High-precision measurement and standard calibration of triple oxygen isotopic compositions ($\delta^{18}O$, $\Delta^{17}O$) of sulfate by F_2 laser fluorination. Chem Geol 440:50–59. https://doi.org/10.1016/j.chemgeo.2016.07.003

Cressy PJ, Bogard DD (1976) On the calculation of cosmic-ray exposure ages of stone meteorites. Geochim Cosmochim Acta 40(7):749–762. https://doi.org/10.1016/0016-7037(76)90028-4

Day JMD, Walker RJ, Ash RD, Liu Y, Rumble D, Irving AJ, Goodrich CA, Tait K, McDonough WF, Taylor LA (2012) Origin of felsic achondrites Graves Nunataks 06128 and 06129, and ultramafic brachinites and brachinite-like achondrites by partial melting of volatile-rich primitive parent bodies. Geochim Cosmochim Acta 81:94–128. https://doi.org/10.1016/j.gca.2011.12.017

Day JMD, Corder CA, Rumble D III, Assayag N, Cartigny P, Taylor LA (2015) Differentiation processes in FeO-rich asteroids revealed by the achondrite Lewis Cliff 88763. Meteorit Planet Sci 50(10):1750–1766. https://doi.org/10.1111/maps.12509

Drouard A, Gattacceca J, Hutzler A, Rochette P, Braucher R, Bourlès D, Team A, Gounelle M, Morbidelli A, Debaille V, Van Ginneken M, Valenzuela M, Quesnel Y, Martinez R (2019) The meteorite flux of the past 2 m.y. recorded in the Atacama Desert. Geology 47(7):673–676. https://doi.org/10.1130/g45831.1

Eberhardt P, Eugster O, Geiss J (1965) Radiation ages of aubrites. J Geophys Res 70(18):4427–4434. https://doi.org/10.1029/jz070i018p04427

Eugster O (1988) Cosmic-ray production rates for ^{3}He, ^{21}Ne, ^{38}Ar, ^{83}Kr, and ^{126}Xe in chondrites based on ^{81}Kr-Kr exposure ages. Geochim Cosmochim Acta 52(6):1649–1662. https://doi.org/10.1016/0016-7037(88)90233-5

Eugster O, Michel T (1995) Common asteroid break-up events of eucrites, diogenites, and howardites and cosmic-ray production rates for noble gases in achondrites. Geochim Cosmochim Acta 59(1):177–199. https://doi.org/10.1016/0016-7037(94)00327-I

Fan Y, Li SJ, Liu S, Peng H, Song GM, Smith T (2022) The distribution of the desert meteorites in China and their classification. Meteorit Planet Sci 57(3):683–701. https://doi.org/10.1111/maps.13789

Freundel M, Schultz L, Reedy RC (1986) Terrestrial ^{81}Kr-Kr ages of Antarctic meteorites. Geochim Cosmochim Acta 50(12):2663–2673. https://doi.org/10.1016/0016-7037(86)90217-6

Gardner-Vandy KG, Lauretta DS, McCoy TJ (2013) A petrologic, thermodynamic and experimental study of brachinites: partial melt residues of an R chondrite-like precursor. Geochim Cosmochim Acta 122:36–57. https://doi.org/10.1016/j.gca.2013.07.035

Goodrich CA, Delaney JS (2000) Fe/Mg–Fe/Mn relations of meteorites and primary heterogeneity of primitive achondrite parent bodies. Geochim Cosmochim Acta 64(1):149–160. https://doi.org/10.1016/S0016-7037(99)00107-6

Goodrich CA, Kita NT, Spicuzza MJ, Valley JW, Zipfel J, Mikouchi T, Miyamoto M (2010) The northwest Africa 1500 meteorite: not a ureilite, maybe a brachinite. Meteorit Planet Sci 45(12):1906–1928. https://doi.org/10.1111/j.1945-5100.2010.01130.x

Goodrich CA, Kita NT, Sutton SR, Wirick S, Gross J (2017) The miller range 090340 and 090206 meteorites: Identification of new brachinite-like achondrites with implications for the diversity and petrogenesis of the brachinite clan. Meteorit Planet Sci 52(5):949–978. https://doi.org/10.1111/maps.12846

Greenwood RC, Franchi IA, Gibson JM, Benedix GK (2012) Oxygen isotope variation in primitive achondrites: The influence of primordial, asteroidal and terrestrial processes. Geochim Cosmochim Acta 94:146–163. https://doi.org/10.1016/j.gca.2012.06.025

Hasegawa H, Mikouchi T, Yamaguchi A, Yasutake M, Greenwood RC, Franchi IA (2019) Petrological, petrofabric, and oxygen isotopic study of five ungrouped meteorites related to brachinites. Meteorit Planet Sci 54(4):752–767. https://doi.org/10.1111/maps.13249

Heber VS, Baur H, Bochsler P, McKeegan KD, Neugebauer M, Reisenfeld DB, Wieler R, Wiens RC (2012) Isotopic mass fractionation of solar wind: evidence from fast and slow solar wind collected by The *Genesis* Mission. Astrophys J 759(2):121. https://doi.org/10.1088/0004-637x/759/2/121

Huss GR, Lewis RS (1994) Noble gases in presolar diamonds. I.: three distinct components and their implications for diamond origins. Meteoritics 29(6):791. https://doi.org/10.1111/j.1945-5100.1994.tb01094.x

Hyde BC, Day JMD, Tait KT, Ash RD, Holdsworth DW, Moser DE (2014) Characterization of weathering and heterogeneous mineral phase distribution in brachinite Northwest Africa 4872. Meteorit Planet Sci 49(7):1141–1156. https://doi.org/10.1111/maps.12320

Johnson JE (1977) Brachina meteorite—A chassignite from South Australia. Records of the South Australian Museum 17:309

Keil K (2014) Brachinite meteorites: partial melt residues from an FeO-rich asteroid. Geochemistry 74(3):311–329. https://doi.org/10.1016/j.chemer.2014.02.001

Kring DA, Boynton WV (1992) The trace-element composition of eagles nest and its relationship to other ultramafic achondrites. In: Proceedings of 23rd lunar and planetary science conference, pp. 727–728.

Krot AN, Keil K, Scott ERD, Goodrich CA, Weisberg MK (2014) Classification of meteorites and their genetic relationships. Treatise on

geochemistry. Elsevier, Amsterdam, pp 1–63. https://doi.org/10.1016/b978-0-08-095975-7.00102-9
Leya I, Masarik J (2009) Cosmogenic nuclides in stony meteorites revisited. Meteorit Planet Sci 44(7):1061–1086. https://doi.org/10.1111/j.1945-5100.2009.tb00788.x
Li SJ, Wang SJ, Bao HM, Miao BK, Liu S, Coulson IM, Li XY, Li Y (2011) The Antarctic achondrite, grove mountains 021663: an olivine-rich winonaite. Meteorit Planet Sci 46(9):1329–1344. https://doi.org/10.1111/j.1945-5100.2011.01232.x
Li SJ, Yin QZ, Bao HM, Sanborn ME, Irving A, Ziegler K, Agee C, Marti K, Miao BK, Li XY, Li Y, Wang SJ (2018) Evidence for a multilayered internal structure of the chondritic acapulcoite-lodranite parent asteroid. Geochim Cosmochim Acta 242:82–101. https://doi.org/10.1016/j.gca.2018.09.004
Li SJ, Leya I, Wang SJ, Smith T, Bao HM, Fan Y, Mo B (2021) Exposure history, petrology, and shock-induced sulfidization reaction of Alatage Mountain 001 strewn field samples. Meteorit Planet Sci 56(7):1293–1310. https://doi.org/10.1111/maps.13710
Matsuda J, Matsumoto T, Sumino H, Nagao K, Yamamoto J, Miura Y, Kaneoka I, Takahata N, Sano Y (2002) The $^{3}He/^{4}He$ ratio of the new internal He Standard of Japan (HESJ). Geochem J 36(2):191–195. https://doi.org/10.2343/geochemj.36.191
McDonough WF, Sun SS (1995) The composition of the Earth. Chem Geol 120(3–4):223–253. https://doi.org/10.1016/0009-2541(94)00140-4
Meunier-Mili N, Kaczmarek MA, Bystricky M (2024) A petrological and microstructural study of ten brachinites: a cumulate texture? J Geophys Res Planets 129(4):e2023JE007998. https://doi.org/10.1029/2023JE007998
Mittlefehldt DW, Bogard DD, Berkley JL, Garrison DH (2003) Brachinites: Igneous rocks from a differentiated asteroid. Meteorit Planet Sci 38(11):1601–1625. https://doi.org/10.1111/j.1945-5100.2003.tb00004.x
Mittlefehldt DW, McCoy TJ, Goodrich CA, Kracher A (1998) Chapter 4. Non-chondritic meteorites from asteroidal bodies. In: Papike JJ (ed) Planetary materials, pp 523–718. https://doi.org/10.1515/9781501508806-019
Nehru CE, Prinz M, Delaney JS, Dreibus G, Palme H, Spettel B, Wänke H (1983) Brachina: a new type of meteorite, not a chassignite. J Geophys Res 88(S01):B237–B244. https://doi.org/10.1029/jb088is01p0b237
Nehru C, Snellenburg JW, Zucker SM, Prinz M (1979) Olivine coronas in mesosiderites: Implications and petrogenesis. In: Proceedings of 10th lunar and planetary science conference, pp 904–906
Nehru CE, Prinz M, Weisberg MK, Ebihara ME, Clayton RN, Mayeda TK (1996) A new brachinite and petrogenesis of the group. In: Proceedings of 27th lunar and planetary science conference, pp 943–944
Nicklas RW, Day JMD, Váci Z, Ren MH, Gardner-Vandy KG, Tait KT (2023) Highly siderophile element fractionation during chondrite melting inferred from olivine-rich primitive achondrites. Geochim Cosmochim Acta 351:66–77. https://doi.org/10.1016/j.gca.2023.04.019
Ott U, Löhr HP, Begemann F (1985) Noble gases and the classification of brachina. Meteoritics 20(1):69–78. https://doi.org/10.1111/j.1945-5100.1985.tb00847.x
Ott U, Lohr PH, Begemann F (1993) Noble gases in Yamato-75097 inclusion: Similarities to brachinites (only?). Antarctic Meteorites XVIII 18:236–239
Patzer A, Schultz L, Franke L (2003) New noble gas data of primitive and differentiated achondrites including Northwest Africa 011 and Tafassasset. Meteorit Planet Sci 38(10):1485–1497. https://doi.org/10.1111/j.1945-5100.2003.tb00252.x
Pourkhorsandi H, Gattacceca J, Rochette P, D'Orazio M, Kamali H, de Avillez R, Letichevsky S, Djamali M, Mirnejad H, Debaille V, Timothy Jull AJ (2019) Meteorites from the lut desert (Iran). Meteorit Planet Sci 54(8):1737–1763. https://doi.org/10.1111/maps.13311
Ranjith PM, He HY, Miao BK, Su F, Zhang CT, Xia ZP, Xie LF, Zhu RX (2017) Petrographic shock indicators and noble gas signatures in a H and an L chondrite from Antarctica. Planet Space Sci 146:20–29. https://doi.org/10.1016/j.pss.2017.08.009
Righter K, Sutton SR, Danielson L, Pando K, Newville M (2016) Redox variations in the inner solar system with new constraints from vanadium XANES in spinels. Am Mineral 101(9):1928–1942. https://doi.org/10.2138/am-2016-5638
Rubin AE (2002) Smyer H-chondrite impact-melt breccia and evidence for sulfur vaporization. Geochim Cosmochim Acta 66(4):699–711. https://doi.org/10.1016/S0016-7037(01)00799-2
Rumble D, Irving A, Bunch T, Wittke J, Kuehner S (2008) Oxygen isotopic and petrological diversity among brachinites NWA 4872, NWA 4874, NWA 4882 and NWA 4969: how many ancient parent bodies? In: Proceedings of 39th lunar and planetary science conference, pp 1974–1975
Ruzicka A, Grossman JN, Garvie L (2014) The meteoritical bulletin, No. 100, 2014 June. Meteorit Planet Sci 49(8):E1–E10. https://doi.org/10.1111/maps.12342
Ruzicka A, Grossman J, Bouvier A, Herd CDK, Agee CB (2015) The meteoritical bulletin, No. 101. Meteorit Planet Sci 50(9):1661. https://doi.org/10.1111/maps.12490
Shuster DL, Cassata WS (2015) Paleotemperatures at the lunar surfaces from open system behavior of cosmogenic ^{38}Ar and radiogenic ^{40}Ar. Geochim Cosmochim Acta 155:154–171. https://doi.org/10.1016/j.gca.2015.01.037
Smith T, He HY, Li SJ, Su F (2023) Light noble gases in 11 achondrites: cosmic ray exposure ages, gas retention ages, and preatmospheric sizes. Meteorit Planet Sci 58(11):1580–1599. https://doi.org/10.1111/maps.14085
Stöffler D, Keil K, Edward RDS (1991) Shock metamorphism of ordinary chondrites. Geochim Cosmochim Acta 55(12):3845–3867. https://doi.org/10.1016/0016-7037(91)90078-J
Swindle TD, Kring DA, Burkland MK, Hill DH, Boynton WV (1998) Noble gases, bulk chemistry, and petrography of olivine-rich achondrites Eagles Nest and Lewis Cliff 88763: comparison to brachinites. Meteorit Planet Sci 33(1):31–48. https://doi.org/10.1111/j.1945-5100.1998.tb01605.x
Tremblay MM, Shuster DL, Balco G (2014) Cosmogenic noble gas paleothermometry. Earth Planet Sci Lett 400:195–205. https://doi.org/10.1016/j.epsl.2014.05.040
Wadhwa M, Shukolyukov A, Lugmcair GW (1998) ^{53}Mn-^{53}Cr systematics in Brachina: A record of one of the earliest phases of igneous activity on an asteroid? In: Proceedings of 29th lunar and planetary science conference, abstract #1480, CD-ROM
Warren PH, Kallemeyn GW (1989) Geochemistry of polymict ureilite EET83309, and a partially-disruptive impact model for ureilite origin. Meteoritics 24(4):233–246. https://doi.org/10.1111/j.1945-5100.1989.tb00698.x